Flow around a 5:1 rectangular cylinder: effects of upstream-edge rounding

B. Rocchio[a], A. Mariotti[a,*], M.V. Salvetti[a]

[a]*Dipartimento di Ingegneria Civile e Industriale, Università di Pisa, Via G. Caruso 8, 56122 Pisa, Italia*

Abstract

A sensitivity analysis of highly-resolved large-eddy simulations of the flow around a 5:1 rectangular cylinder to the introduction of a small rounding of the upstream edges is presented. Different values of the edge radius of curvature are considered, in a range such that they might reasonably be ascribed to manufacturing tolerances. A stochastic approach is adopted in order to build response curves of the quantities of interest as a function of the radius of curvature. The considered computational set-up, characterized by a fine numerical resolution and a low subgrid-scale (SGS) dissipation, predicts for the body having perfectly sharp edges a short mean recirculation length on the cylinder side, in disagreement with experimental data. On the other hand, even for the smallest considered radius of curvature, the length of the mean recirculation region increases significantly and, hence, the agreement with the experimental data is much improved. It is observed that the sharp edge introduces a higher level of turbulent fluctuations in

*Corresponding author

Email addresses: benedetto.rocchio@ing.unipi.it (B. Rocchio), alessandro.mariotti@for.unipi.it (A. Mariotti), mv.salvetti@ing.unipi.it (M.V. Salvetti)

the shear-layer at separation, which, if not artificially damped by numerical or SGS dissipation, grows faster and leads to a further upstream roll-up of the shear-layers and, hence, to a shorter mean recirculation region than in simulations with rounded edges.

Keywords: BARC benchmark, rectangular cylinder, Large-Eddy Simulations, Upstream edge rounding

1. Introduction

The flow around elongated rectangular cylinders is of interest in civil engineering, because it can be considered a model problem for instance for tall buildings or bridge sections. Among the possible chord to depth ratios, the

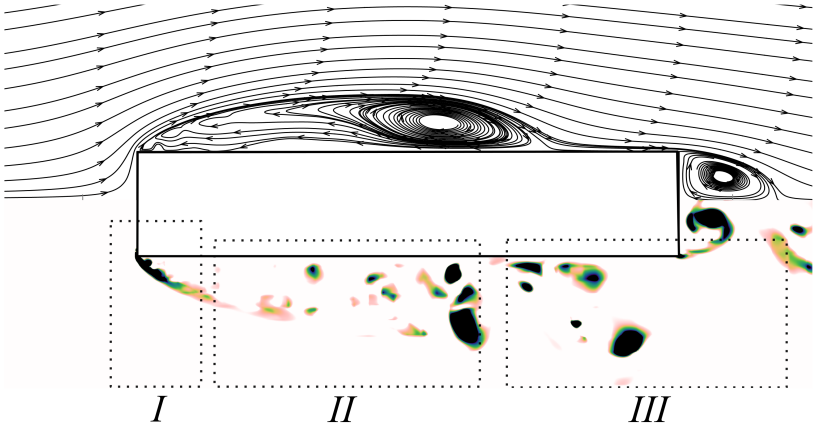

Figure 1: Qualitative behavior of the BARC flow. Top part: mean streamlines; bottom part: instantaneous vorticity.

aspect ratio of 5:1 is the focus of an international benchmark, launched in 2008 [1] and known in literature as BARC (Benchmark on the Aerodynamics of a Rectangular Cylinder). Despite its simple geometry, the BARC config-

uration is characterized by a quite complex flow, as qualitatively shown in Fig. 1. The boundary layer, developing on the front face, separates from the upstream edges becoming a separated shear-layer (region I in Fig. 1). Then, the shear-layer starts to roll-up forming vortical structures of different size (region II). The corresponding mean flow is depicted in the top part of Fig. 1; it is characterized by a recirculation region ending by mean flow reattachment close to the trailing edge (region III). Furthermore, downstream in the wake the classical vortex shedding occurs. A peculiar feature of BARC was that no reference data were available, rather the results of different experimental studies were collected as well as of different numerical simulations. A review of the experimental and numerical contributions to BARC up to 2014 can be found in Bruno et al. [2]. More recent works on BARC are also present in the literature (see e.g. [3–8]).

Bruno et al. [2] pointed out a significant dispersion in the results for the flow and the pressure distribution over the cylinder lateral sides, and, hence, for the oscillating lift as well, both in experiments and numerical simulations. No conclusive explanation for this dispersion was possible from the data reviewed in Bruno et al. [2].

As for experiments, the more recent study by Mannini et al. [4] clearly shows how the features of the mean flow and the pressure distribution on the cylinder side are highly sensitive to the freestream turbulence. They show how by increasing the incoming turbulence the mean pressure coefficient on the cylinder side increases upstream and the peak of its standard deviation is shifted upstream compared to the case of smooth flow. As shown by Kiya et al. [9], the maximum value of the pressure coefficient standard deviation is

related to the mean flow reattachment location. Therefore, by increasing the value of the incoming turbulence, the length of the mean recirculation region on the cylinder side decreases. Since the different experimental contributions to BARC were carried out in different facilities with different freestream turbulence levels, this may explain the dispersion of the experimental data.

On the other hand, the sensitivity analyses carried out to investigate the reasons of the dispersion of numerical results not only were not conclusive, but they led to unexpected findings. As a first example, Bruno et al. [10] carried out different LES simulations by changing the grid resolution. It turned out that the increase of the grid resolution in the spanwise direction, i.e. along the cylinder axis, leads to a significant reduction of the mean recirculation region length, which becomes shorter than the range of the predictions of the experimental and numerical contributions to BARC. This finding was recently confirmed in [5] by a stochastic analysis of the sensitivity of LES results to grid resolution in the spanwise direction and to the amount of subgrid scale (SGS) dissipation. Indeed, it was observed that numerical simulations, characterized by a finer grid resolution or/and by lower SGS dissipation, tend to underestimate significantly the distance from the upstream edges at which the mean flow reattachment occurs. It must be pointed out that Bruno et al. [10] and Mariotti el al. [5] reach the same conclusions by employing two different numerical codes and methods and different SGS models. A similar behavior was also observed by Mannini et al. [11] in Detached-Eddy Simulations when decreasing the numerical viscosity. Thus, these studies lead to a sort of "paradox": simulations which are a-priori highly accurate (fine grid resolution and limited numerical and

SGS dissipation) give results in strong disagreement with those of the other simulations and with experiments. The disagreement with the numerical contributions reviewed in Bruno et al. [2] can be explained following the analysis in [5], which shows that highly-resolved and low-dissipation LES predict a roll up of the detaching shear-layer close to the upstream edges, leading to the formation of very small vortical structures. Thus, it can be argued that URANS and hybrid URANS-LES simulations and also LES with too coarse grid resolutions or too large dissipation, as most of those reviewed in Bruno et al. [2], cannot capture these small vortical structures and hence they can not accurately reproduce the dynamics of the flow features on the cylinder side.

However, more surprisingly, the results of "high-fidelity" simulations deviate also from experimental data, which predict a longer mean recirculation region. In this case, the discrepancy might be due to some differences between the experimental and the numerical set-up. First, let us consider the inlet conditions. Most of the numerical simulations collected in the literature, including those in Bruno et al. [10] and Mariotti et al. [5], are performed without considering any turbulence at the inlet of the computational domain, while in experiments the incoming velocity is always characterized by a certain degree of turbulence. However, as shown in Mannini et al. [4], by increasing the incoming turbulence intensity the length of the mean recirculation region on the cylinder side decreases. Since, the numerical simulations have no turbulence at the inlet, the mean recirculation bubble length should be longer than the one in the experiments, while the results of "high-fidelity" simulations show the opposite tendency. Another source of discrepancy are

the periodic boundary conditions used in the spanwise direction in the simulations to mimic an infinite cylinder, while in the experiments long prismatic models are used together with ad-hoc techniques to reduce three-dimensional effects. However, Bruno et al. [10] show how the effect on the size of the mean recirculation bubble of the spanwise length of the cylinder together with periodic boundary conditions is almost negligible. Another difference between numerical simulations and experiments concerns the sharpness of the upstream edges of the cylinder. Indeed, in the simulations perfectly sharp edges are considered while in the experiments the real geometry has some uncertainty due to the manufacturing tolerances, which depend on the process used to produce the body. Thus, the experimental model has always a certain degree of rounding in the upstream and downstream edges. The effects of rounded edges have been quite extensively investigated for square cylinders at different Reynolds numbers and for different radii of curvature (see e.g. [12–14] and the references therein). However, to the best of our knowledge, this issue has not been addressed for elongated rectangular cylinders, characterized by mean flow reattachment on the side. The effect of the edge rounding on the flow over a semi-infinite 2D halfbody was investigated in Lamballais et al. [15] for a Reynolds number significantly lower than the one of the present study and for larger radii of curvature.

The present work is indeed aimed at studying the effects of a small rounding of the upstream edges of the BARC geometry and at investigating whether this may explain the discrepancies between "high-fidelity" simulations and experiments. To this aim, we adopt the same modeling, numerical method and computational set-up of one of the simulations in Mariotti et

al.[5], which predicts a short mean recirculation region, and a small rounding of the upstream edges of the body is introduced. Different values of the curvature radius, r, are considered; the range of variation has been chosen in order to contain reasonable values, which might be ascribed to manufacturing tolerances. In order to build response curves of the quantities of interest as a function of the curvature radius, a stochastic approach is adopted, in which r has uncertain values, and the response curves are built through the generalized polynomial chaos (gPC) expansion [16].

2. Methodology

2.1. Numerical discretization and simulation set-up

LES simulations are carried out for the incompressible flow around a fixed rectangular cylinder with a chord-to-depth ratio, B/D, equal to 5 at zero angle of attack. All the quantities are made dimensionless by using the cylinder height (D), the fluid density (ρ) and the freestream velocity (U_∞).

The simulations are carried out through the open-source code, Nek5000, based on a high-order accurate spectral-element method [17]. Each spectral element is rectangular, or a suitable coordinate mapping of a rectangle. The basis functions inside each element consist of Legendre polynomials of order N for velocity, and $N-2$ for pressure. The order of the Legendre polynomials used as basis functions inside each element is kept herein constant equal to $N = 6$, as in Mariotti et al. [5]. It can be shown that the method has a spectral convergence in N (so-called p-refinement), and the convergence of a high-order finite-element method in the number of elements (h-refinement). The time discretization in Nek5000 is based on the high-order

splitting method developed in [18]. Here, a third-order backward differentiation scheme is used for the time derivatives. The viscous terms are treated implicitly while an explicit scheme is considered for the non linear convective terms, with a third order forward extrapolation in time.

A low-pass explicit filter in the modal space is applied at the end of each step of the Navier-Stokes time integration [19]. The adopted filter is a sharp cut-off one for the modes up to the unfiltered ones (k_c), here equal to $N-3$, and it has a quadratic transfer function for the modes inside $k_c \leq k \leq N$. The transfer function of the filter can be written as follows:

$$\begin{cases} \sigma_k = 1 & k < k_c \\ \sigma_k = 1 - w\left(\frac{k-k_c}{N-k_c}\right)^2 & k_c \leq k \leq N \end{cases} \tag{1}$$

where w is a tunable weighting parameter. This modal filter provides a dissipation in the highest resolved modes, which is usually interpreted as a SGS dissipation [20][21].

The computational domain is sketched in Fig. 2. It is rectangular with $-15.5 \leq x/B \leq 25.5$, $-15.1 \leq y/B \leq 15.1$, where x and y denote the streamwise and wall-normal directions, respectively, and the cylinder center is located at $x = y = 0$. The spanwise domain size is equal to B. The computational domain has the same dimensions as the one used in [5] and in some LES contributions to BARC reviewed in [2].

A uniform velocity profile is imposed at the inflow (no turbulence), while no-slip conditions are applied at the solid walls. Periodic conditions are imposed in the spanwise direction, while traction-free boundary conditions are used at the outflow and on the remaining lateral sides of the computational domain. Finally, the Reynolds number based on the free-stream velocity and

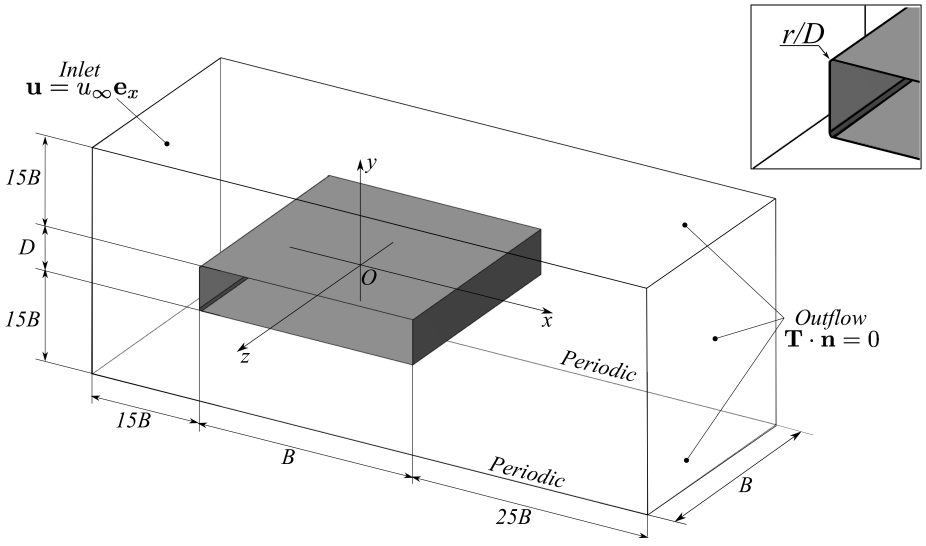

Figure 2: Sketch of the computational domain with the boundary conditions.

on the cylinder depth, Re, is equal to 40000.

The spectral element size in the streamwise and and lateral directions near the cylinder is $\Delta x = \Delta y = 0.125D$, while in the spanwise direction is $\Delta z = 0.558D$. The weight of the explicit filter, $w = 0.05$. These values are the same as in one of the 13 simulations in [5] having a short mean recirculation region. In the simulation with rounded upstream edges, the computational grid is the same as in the sharp-edge case except that the rounded part is handled by curvilinear elements.

The time step, made non dimensional by the freestream velocity and D, is equal to 0.003 and it corresponds to approximately 3000 time steps in each vortex-shedding cycle.

2.2. Stochastic sensitivity analysis

A stochastic approach, based on generalized Polynomial chaos [16] has been adopted to systematically quantify the effects of edge rounding starting from a few deterministic simulations. The value of the curvature radius of the upstream edges is therefore considered as an uncertain parameter and it is allowed to vary in the range $r/D \in (0, 0.054)$. This interval has been chosen in order to contain reasonable values of the curvature radius, which might be ascribed to manufacturing tolerances. For this parameter the PDF is taken as uniform, implying the use of the Legendre polynomials in the gPC expansion. The choice of this input PDF is motivated by the fact that, among the classically used distributions, it is the least informative one with the highest variance in given intervals. Therefore, for a given variation interval of the input parameter, the uniform PDF distribution is expected to give the largest variability of the output quantities, providing a conservative estimation of the sensitivity to the considered input. Through this approach a generic quantity of interest can be written as a truncated projection over an orthogonal basis:

$$R(\gamma) = \sum_{k=0}^{T} a_k \Phi_k(\boldsymbol{\xi}(\gamma)) \tag{2}$$

with γ being a random event and $\boldsymbol{\xi}(\gamma) = [\xi_1, \xi_2, ..., \xi_M]$ the $M-$dimensional vector consisting of the independent random variables, $\Phi_k(\boldsymbol{\xi})$ is the gPC polynomial of index k and a_k is the corresponding Galerkin projection coefficient. The truncation index $T = \prod_{j=1}^{M}(P_j + 1) - 1$ depends on the number of parameters (M) and on the maximum order of the polynomial for each

parameter. The coefficients of the gPC expansion are evaluated as follows:

$$a_k = \frac{(R \cdot \Phi_k)}{(\Phi_k \cdot \Phi_k)} \tag{3}$$

where $(* \cdot *)$ denotes the usual L_2 scalar product involving a weight function depending on the chosen polynomial family. The integrals in the scalar products are computed herein numerically by using Gaussian quadrature with $(P+1)^M$ quadrature points, which are defined according to the chosen polynomial family. For each quadrature point a deterministic computation must be carried out. Since we adopt herein $P = 3$ and M is equal to 1, thus 4 quadrature points are needed to numerically compute the gPC coefficients (see Equation (2)). For each quadrature point, shown in Table 1, a deterministic LES simulation has to be performed. The convergence of the truncated gPC expansion was a-posteriori assessed by checking that the contribution of the polynomials of highest order remains very low for all the considered quantities (not shown here for the sake of brevity).

Table 1: Quadrature points for the sensitivity analysis to curvature radius (r/D).

Range	$1^{st}point$	$2^{nd}point$	$3^{rd}point$	$4^{th}point$
$(0; 0.054)$	0.0037	0.0177	0.036	0.05

The impact of the uncertainty in r/D is evaluated on the quantities of interest such as the length of the mean recirculation region on the cylinder side and the distribution on the cylinder lateral surface of the time- and span-averaged pressure coefficient and of its standard deviation.

3. Results and discussion

In this section the results of the stochastic sensitivity analysis are presented and compared with the ensemble average of the BARC experiments, the recent experiments in [4] (those with the lowest intensity of inlet turbulence) and with the numerical solution obtained by Mariotti et al. [5] for perfectly sharp edges with the same numerical methodology and computational set-up.

Let us first consider the distribution on the lateral surface of the cylinder of the pressure coefficient, which is defined as follows:

$$C_p = \frac{p - p_\infty}{1/2\rho U_\infty^2} \tag{4}$$

where p is the local pressure, ρ is the density and p_∞ and U_∞ are the freestream pressure and velocity respectively. The average of C_p in time, in the spanwise direction and between the upper and lower half perimeters of the cylinder is denoted as $\langle C_p \rangle$; the standard deviation, $\sigma(C_p)$ is also computed by the same averaging procedure. The local abscissa, s/D, is the distance from the cylinder stagnation point, which is located at $x = -B/2$, $y = 0$ and $z = 0$, measured along the cylinder side. The mean pressure coefficient $\langle C_P \rangle$ distributions for the LES simulations (one for each quadrature point reported in Table 1) are shown in Fig. 3a. They are compared with the results for the simulation with sharp-edge in [5], with the ensemble statistics of the BARC experiments (from [2]) and with the experimental data in [4]. The BARC ensemble statistics are given in terms of median, 25th and 75th percentile values, p_{25} and p_{75}, (boxes), whiskers (bars) and outliers (crosses), if any. Points are drawn as outliers if they are larger than $p_{75} + \beta(p_{75} - p_{25})$

or smaller than $p_{25} - \beta(p_{75} - p_{25})$, $\beta = 1.5$ being the maximum whisker length. The introduction of a curvature radius at the upstream edges leads to an enhanced agreement with the experimental data. It is remarkable, how even the smallest curvature radius ($r/D = 0.0037$ ($\bigcirc$)), which would be hard to be detected in experiments unless ad-hoc diagnostic techniques are employed, is able to completely change the $\langle C_P \rangle$ distribution compared to sharp-edge simulation ($r/D = 0$ (- -)). For $r/D = 0.0037$, the plateau region is significantly longer and the position at which the pressure coefficient starts to recover is moved downstream compared to the sharp edge simulation. By further increasing the curvature radius the pressure coefficient distribution does not change much, even though the growth of $\langle C_P \rangle$ is slightly shifted at higher s/D. The PDF of the averaged pressure coefficient, see Fig. 3b, confirms that the variability of $\langle C_P \rangle$ with the edge curvature radius is rather small, with most of the values leading to distributions falling in a very narrow interval, which are very far from that obtained for perfectly sharp edges.

Similar considerations can be done for the standard deviation of the pressure coefficient $\sigma(C_P)$ along the lateral side of the cylinder, shown in Fig. 4. The same comparisons as in Fig. 3 are reported. Once again, the agreement with the experiments improves by introducing a rounding of the upstream edges. The peak of $\sigma(C_P)$ for the sharp-edge simulation [5] is closer to the upstream edge, while for the simulations with rounded edges this peak is moved downstream. Also for this quantity, there is a large difference between the distribution with sharp edges and those with rounded edges, also for the smallest value of r/D. Once again, by increasing the value of r/D the distribution does not change too much. The PDF of $\sigma(C_P)$ is quite

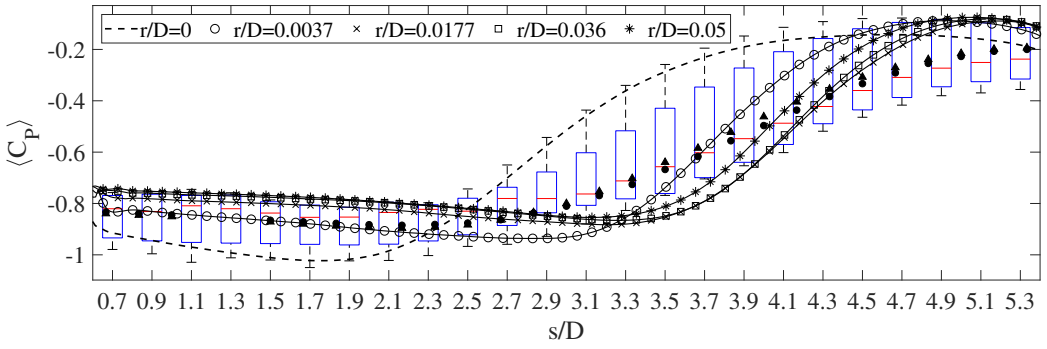

(a)

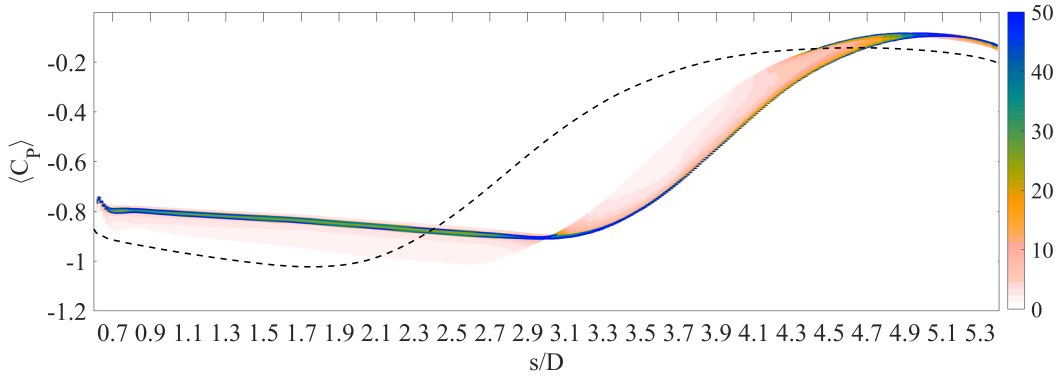

(b)

Figure 3: (a) Mean pressure coefficient comparison between the reference case (- -) [5], experimental data and the deterministic simulations for each quadrature point; (b) PDF of the mean pressure coefficient.

narrow, except for the zone in the downstream part of the lateral surface (Fig. 4b) as a consequence of the previously described variability of the peak with the curvature radius. However, once again the distribution obtained for the sharp edge is far from the range of values which can be expected with rounded edges for varying r/D.

The distributions of the mean C_p and of its standard deviation are related to the mean flow topology on the cylinder side (see e.g. [2, 5]). In particular,

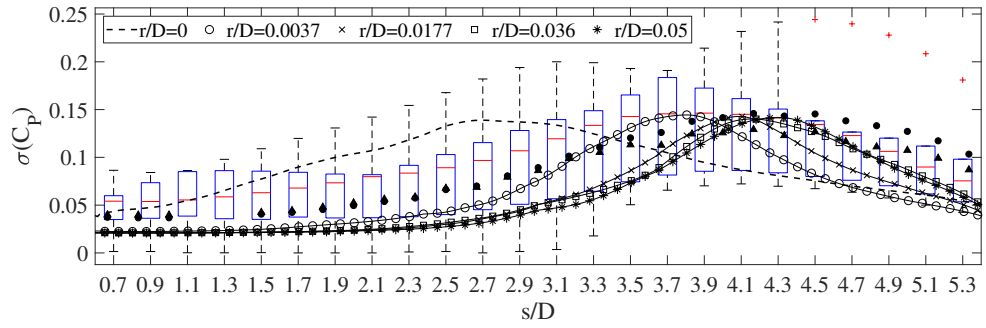

(a)

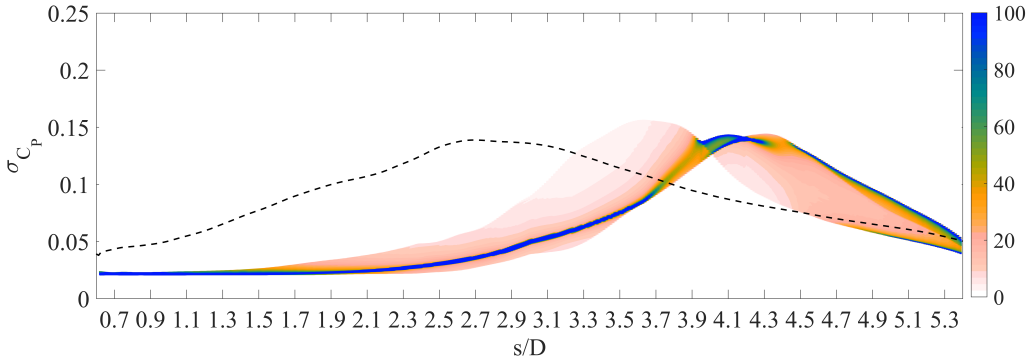

(b)

Figure 4: (a) Standard deviation of the pressure coefficient comparison between the reference case (- -) [5], experimental data and the deterministic simulations for each quadrature point; (b) PDF of the standard deviation of the pressure coefficient.

the location of the recovery of the mean pressure coefficient and of the peak of its standard deviation roughly correspond to the change of curvature of the streamlines bounding the mean recirculation region, and, hence, they are connected with the position of the mean reattachment point on the cylinder lateral surface. The sharp-edge simulation shows a recovery of $\langle C_P \rangle$ and a peak of the $\sigma(C_P)$ both occurring further upstream than in experiments;

consistently, the reattachment of the mean flow also occurs upstream and, hence, the mean recirculation region on the cylinder side is shorter. Figure 5 shows the time- and span-averaged streamlines for the sharp-edge simulation (Fig. 5a) and for the simulations having different curvature radius of the upstream edges (Figures 5b-5e). Coherently with the pressure distribution, each simulation with $r/D > 0$ shows a mean recirculation zone on the lateral surface longer than the one predicted by the sharp-edge one. Again, the largest differences are between the smallest quadrature point, $r/D = 0.0037$, and the sharp-edges case, while by increasing the curvature radius the length of the mean recirculation zone does not show remarkable differences.

To better quantify the sensitivity of the length of the recirculation region to the curvature radius of the upstream edges, the stochastic sensitivity analysis has been carried out for the x location of the reattachment point (x_r) of the mean flow, measured from the center of the cylinder. Fig. 6 shows the PDF of x_r, together with the deterministic results for the simulations with different curvature radius and the one for the simulation with sharp edges. The values obtained in the experiments by [23] and [8] are also reported for comparison. By comparing the deterministic values of x_r, obtained for the different quadrature points in the parameter space, with the experimental values, the best agreement is obtained for $r/D = 0.0037$. The other values of the curvature radius give slightly greater values of x_r. The PDF confirms that, except for the smallest value, the variability of x_r with r/D is very small, as previously observed for the pressure distribution. Finally, the value of x_r given by the sharp-edge simulations is dramatically different from those of the simulations with rounded edges and from the experiments.

The previous results have pointed out how the introduction of a rounding of the upstream edges moves downstream the location at which the mean flow reattaches on the lateral surface of the cylinder, increasing thus the length of the mean recirculation region. It has been shown in [5] that the length of the mean recirculation region is related to the dynamics of shear-layers detaching from the upstream edges. Figure 7 shows the different vortical structures for the simulation with sharp edges, the smallest and the largest values of the curvature radius used for the simulations with rounded edges. The λ_2-criterion is used. Based on this criterion, a vortex can be identified by a connected fluid region in which the second largest eigenvalue of the 3×3 tensor Q is negative, i.e. where $\lambda_2 < 0$. The tensor Q is symmetric and defined as $Q = \Omega \cdot \Omega + E \cdot E$, where Ω and E are respectively the antisymmetric and the symmetric part of the velocity gradient. The shear-layers detaching from the perfectly-sharp edges, $r/D = 0$ (see Fig. 7a), roll-up and form small three-dimensional vortical structures close to the separation point, which are visible by looking at the isosurfaces of the instantaneous vortex indicator λ_2 and at its distribution in the plane $z = 0$. This leads, as previously discussed, to a short mean recirculation region on the cylinder surface, as also shown from the time-averaged λ_2 isosurfaces. When a rounding of the upstream edges is introduced, the detached shear-layers are coherent up to a further downstream position, after which they start to roll-up forming once again small vortical structures. This more downstream roll-up of the shear-layers leads to longer mean recirculation regions, as previously observed and as also shown by the mean λ_2 isosurfaces.

Thus, the previously discussed effects of the introduction of the edge

rounding on the mean flow topology and on the pressure distribution may be explained by the fact that the separated shear layers roll-up and loose coherence more downstream than in the sharp-edge case. To further investigate the evolution of the shear layers, Figure 8 shows the vertical position of the shear-layer external edge and the turbulent kinetic energy along it for the simulations having sharp and rounded upstream edges. It should be pointed out that the word TKE (turbulent kinetic energy) is not fully appropriate for the considered flow region, in which turbulence is not yet fully developed; it is rather a kinetic energy associated to velocity fluctuations. However, the term TKE is used, by following similar works (see e.g. Moore et al. [8] and Lamballais et al. [15]). The external edge of the shear-layer is identified as the vertical distance from the wall at which the mean velocity profile at the considered s reaches its maximum value. Close to the upstream cylinder edge, $s/D = 0.5$, or $x/D = -2.5$, the shear-layer edges have practically the same location in all cases, while different trends are observed moving downstream, which reflect the previously highlighted differences in the shear-layer evolution. By looking at the evolution of the TKE along the shear-layer edge, shown in Fig. 8b, it is evident that for sharp-edge case (- -) it grows much faster than for the cases with rounded edges. Therefore, one may argue that the further upstream roll-up of the shear-layer, and consequently the shorter length of the mean recirculation region, of the sharp-edge case are related with the faster TKE growth. In order to check this assumption, Figure 9 shows the s coordinate of the maximum of TKE versus the location of the mean flow reattachment. All the data collapse nicely on a straight line, confirming thus the correlation between the evolution of TKE along the

shear-layer and the length of the mean recirculation region. By considering the TKE evolution at different vertical locations inside the shear-layer, as e.g. those corresponding with the 90% or 50% of the maximum velocity, similar results are obtained (not shown here for the sake of brevity).

One may wonder now whether the different growth of the TKE along the shear-layer edge may be due to a different global amount of TKE introduced at the edges.

It is possible to quantify the global amount of TKE introduced in the shear-layer by computing the integral of the turbulent kinetic energy (Q) at the section corresponding to the edge of the cylinder $x/D = -2.5$, or $s/D = 0.5$. The integral of the TKE along the local abscissa is defined as follows:

$$\begin{cases} Q(y) = \int q(x,y)dx & 0 \leq s/D < 0.5 \\ Q(x) = \int q(x,y)dy & s/D \geq 0.5 \end{cases} \tag{5}$$

The integrals in Equation 5 are computed from the wall to the edge of the computational domain. In Table 2 the values of Q are reported for the perfectly sharp-edge and rounded-edge simulations, together with the contributions of $\langle u'u' \rangle$, $\langle v'v' \rangle$ and $\langle w'w' \rangle$ to the integrals in Equation (5), named $Q_{\langle u'u' \rangle}$, $Q_{\langle v'v' \rangle}$ and $Q_{\langle w'w' \rangle}$. The amount of energy at the separation point for all the simulations with rounded edges is indeed much smaller than the energy contained in the shear-layer detaching from the sharp-edges. For cases up to $r/D = 0.037$, the amount of TKE introduced in the detaching shear-layer monotonically decreases with increasing r/D, while for $r/D = 0.05$ it increases again, remaining though approximately two order of magnitudes lower than in the sharp-edge case. By looking at the second and third rows

of Table 2, it is interesting to note how for the sharp-edge case the predominant contribution to Q is that related to $\langle v'v' \rangle$, while for all cases up to $r/D = 0.037$ the contribution of the horizontal velocity fluctuations is the largest one, the two contributions being comparable for $r/D = 0.05$.

Table 2: Integral of the turbulent kinetic energy and its contributions at $x/D = -2.5$

r/D	0	0.0037	0.0177	0.036	0.05
Q	$1.4 \cdot 10^{-3}$	$9.0 \cdot 10^{-5}$	$2.99 \cdot 10^{-5}$	$2.47 \cdot 10^{-5}$	$4.26 \cdot 10^{-5}$
$Q_{\langle u'u' \rangle}$	$4.7 \cdot 10^{-5}$	$6.04 \cdot 10^{-5}$	$1.85 \cdot 10^{-5}$	$1.55 \cdot 10^{-5}$	$2.03 \cdot 10^{-5}$
$Q_{\langle v'v' \rangle}$	$8.7 \cdot 10^{-4}$	$2.96 \cdot 10^{-5}$	$1.14 \cdot 10^{-5}$	$9.2 \cdot 10^{-6}$	$2.23 \cdot 10^{-5}$
$Q_{\langle w'w' \rangle}$	$7.9 \cdot 10^{-7}$	$2.3 \cdot 10^{-7}$	$7.4 \cdot 10^{-8}$	$3.9 \cdot 10^{-8}$	$5.1 \cdot 10^{-8}$

The previous results indicate, thus, that the presence of a perfectly sharp edge introduces a large amount of TKE in the shear-layers at separation, which in highly-resolved LES is not damped by numerical or SGS dissipation. This can explain thus the faster growth of TKE along the shear-layer, which is in turn related with a short mean recirculation region.

The behavior of Q and of its contributions, $Q_{\langle u'u' \rangle}$, $Q_{\langle v'v' \rangle}$ and $Q_{\langle w'w' \rangle}$, are plotted in Figure 10 and Figure 11, respectively, as a function of s/D, starting from the stagnation point ($s/D = 0$). It can be seen that for the sharp edge case, Q starts to significantly grow on the front face before the edge and that the main contribution to this growth is given by the $\langle v'v' \rangle$, which are the fluctuations of the velocity component parallel to the wall on the front face. For all the considered cases with rounded edges, the level of velocity fluctuations on the front face is always very low. Note that, on the other hand, the mean velocity behavior in the boundary layer on the front face does

not change significantly when edge rounding is introduced (not shown here for the sake of brevity). After the corner, for the sharp edge case, Q decreases and this is due to a decrease of the $Q_{\langle v'v' \rangle}$ component, while the component $Q_{\langle u'u' \rangle}$ starts to slightly increase. After $s/D = 0.6$ ($x/D = -2.4$) both components of TKE significantly increase moving downstream. Conversely, for the rounded edge cases, the increase of Q occurs more downstream and it is slower than in the sharp-edge case. This is consistent with the evolution of TKE over the shear-layer edge previously shown in Fig. 8b. Moreover, it can be seen that the increase of Q is due to the $Q_{\langle u'u' \rangle}$ contribution, while $Q_{\langle v'v' \rangle}$ and $Q_{\langle w'w' \rangle}$ remain always very low.

The evolution of the TKE can be further analyzed by looking at the production term in the TKE governing equation, $\mathcal{P}$, which for the considered 2D incompressible mean flow can be written as follows:

$$-\mathcal{P} = \langle u'u' \rangle \frac{\partial U}{\partial x} + \langle u'v' \rangle \left(\frac{\partial U}{\partial y} + \frac{\partial V}{\partial x} \right) + \langle v'v' \rangle \frac{\partial V}{\partial y} \tag{6}$$

Equation (6) shows how the turbulent kinetic energy production is related to turbulent fluctuations and to the mean shear. Moore et al. [8] discussed how the second term in the RHS of Equation (6) is much lower compared to the other two. Following this result, we only consider the first and third term in the RHS of Equation (6).

Figure 12 shows the profiles of the two contributions to the opposite of the TKE production, $-\mathcal{P}$, for the simulations with sharp-edge and for the different values of the curvature radius at different streamwise positions. We focus the analysis in the upstream part of the body, $-2.5 \leq x/D \leq -2.1$, just after flow separation. At $x/D = -2.5$, only the simulation with the sharp edge shows non-zero values of the two components. At $x/D =$

-2.5, for the sharp-edge case, the largest contribution to $\mathcal{P}$ is that of the last term in Equation (6). This is consistent with the previous observation that $\langle v'v' \rangle$ is the largest contribution to TKE at this location. Moreover, it is a negative production term, leading thus to the destruction of TKE. Negative TKE production was also found in the initial part of the shear layer by Cimarelli et al. [24] at significantly lower Reynolds number. However, moving downstream the contribution of the first term in the RHS of Equation (6) starts to grow and becomes the predominant one. This is a positive production term, and, hence, the total production becomes positive, as it can be seen in Fig. 13 in which $-\mathcal{P}$ is shown, leading to the previously observed growth of TKE along the shear-layer edge. By comparing Fig. 13 and Fig. 8a, it can be noticed that the peak of TKE production is indeed located approximately at the shear-layer edge. A similar behavior of the production of TKE along the shear-layer was also found in the experiments by Moore et al. [8]. As for the cases with rounded edges, the contribution to $\mathcal{P}$ of the last term in Equation (6) always remains negligible, while the first one starts to be appreciable at the considered sections only for the cases with the smallest roundings. However, the global production in all cases remains much slower than for the sharp-edge simulation, consistently with the previously observed slower increase of Q and of the TKE along the shear-layer.

In order to further investigate on the dynamics of the shear layers detaching from the upstream edges, the instantaneous vortex indicator λ_2 on the plane $z = 0$ is compared at different times for $r/D = 0$ and $r/D = 0.0037$ in Fig. 14. These zoomed images (and the attached videos) of vortical structures better show the corrugation and the roll-up of the shear layers, which

lead to the increase of fluctuating energy observed in the separated shear layer on the cylinder side for both cases.

The fact that the increase of TKE along the separated shear layers is related with the Kelvin-Helmholtz instability is confirmed by the frequency analysis of the time velocity signals, which was carried out herein through the wavelet transform for a few locations slightly outside the averaged shear-layer external edges at different longitudinal positions in the interval $x/D = [-2.5; 0]$, as summarized in Table 3. The wavelet spectra for the simulations having $r/D = 0$ and $r/D = 0.0037$ are reported in Fig. 15a and Fig. 15b, respectively, whereas probe positions in relation to the time-averaged shear-layer edges are sketched inFigure 15c. The spectra are derived from the wavelet transform of the x-velocity signals, by integrating in time the wavelet maps obtained by employing the complex Morlet wavelet $\psi(t) = e^{(i\omega_0 t)}e^{(t^2/2)}$ and using a central frequency $\omega_0 = 6\pi$. This procedure permits us to obtain spectra that are smoother than the Fourier ones and well defined from the mathematical point of view (see e.g. [25–27] for further details on the wavelet procedure). The frequencies are expressed in non-dimensional form through the Strouhal number $St = fD/U_\infty$. As can be observed, a clear peak is found in the spectra for $-2.5 \leq x/D \leq -2.0$ for the case $r/D = 0$ (see the spectra (1)-(3) in Fig. 15a) and for $-2.3 \leq x/D \leq -1.5$ for the case $r/D = 0.0037$ (see (2)-(4) Fig. 15b) at frequencies $St_{KH} = 1.52$ and $St_{KH} = 0.88$ for $r/D = 0$ and for $r/D = 0.0037$, respectively, which are typical Kelvin-Helmholtz frequencies if rescaled with the local width of the shear layer. The maximum spectral power density for these peaks is found at $x/D = -2.3$ for $r/D = 0$ and $x/D = -2$ for $r/D = 0.0037$, which are slightly upstream of the

location at which the roll up of the shear layer mainly occurs, as can be seen in Fig.14. Moving downstream, peaks at $St_{KH/2}$ and $St_{KH/4}$ in the wavelet spectra of the velocity signals are present, due to pairing of the vortical structure originating from the sear-layer roll up (see e.g. [8, 28]). In the wake signals (not shown here), vortex-shedding fluctuations at $St_{VK} = 0.153$ and $St_{VK} = 0.119$ are found for $r/D = 0$ and for $r/D = 0.0037$, respectively. These frequencies are not observed in the signals shown in Figs. 15a and 15b indicating that the vortex shedding in the near wake does not influence the dynamics of this first part of the shear layers, as also found in [8].

Based on the previous analysis, it is then reasonable to infer that the Kelvin-Helmholtz phenomena explain the increase of TKE along the separated shear layer, but not that occurring on the front face and around the corner in the sharp-edge case. The fact that the fluctuating energy in this region is not due to the effect of the phenomena downstream is also supported by the observation that the TKE has a peak around the corner, then it decreases to increase once again due to the effect of the Kelvin-Helmholtz phenomena (see Fig. 10). On the other hand, the velocity fluctuations on the front face do not seem to be related to the transition of the boundary layer, whose characteristic thicknesses are shown in Fig. 16 for all the considered cases. It can be seen that near the stagnation point and in the first part of the front face ($s/D < 0.3$) there are no appreciable differences among the different cases in both the displacement and momentum thicknesses, while the results become different in the region where the boundary layer is affected by the pressure gradients, which are related with the curvature of the flow near the upstream edge and, thus, with the edge rounding. Nonetheless, in

all cases no evidence of transition is observed. This confirms the previous hypothesis that the velocity fluctuations found on the front face of the cylinder for r/D are in some way related with the presence of a perfectly sharp edge and that, this in turn, might trigger the Kelvin-Helmholtz instability more upstream leading to the previously discussed effect on the mean flow topology.

Table 3: Probe positions for the wavelet spectra.

$r/D = 0$		$r/D = 0.0037$	
probe (1)	$(-2.5, 0.7)$	probe (1)	$(-2.5, 0.7)$
probe (2)	$(-2.3, 0.8)$	probe (2)	$(-2.3, 0.8)$
probe (3)	$(-2.0, 1.0)$	probe (3)	$(-2.0, 1.0)$
probe (4)	$(-1.5, 1.2)$	probe (4')	$(-1.5, 1.1)$
probe (5)	$(-1.0, 1.4)$	probe (5')	$(-1.0, 1.2)$
probe (6)	$(-0.5, 1.5)$	probe (6')	$(-0.5, 1.3)$
probe (7)	$(0.0, 1.6)$	probe (7')	$(0.0, 1.4)$

4. Concluding remarks

The LES simulations of the BARC benchmark carried out with rounded upstream edges for small values of the curvature radius and the related stochastic sensitivity analysis have shown that the flow features on the cylinder side are significantly different from those obtained in LES with sharp edges. This occurs even for very small values of r/D, which are difficult to be detected in experimental models, unless ad-hoc diagnostics are employed. In particular, the length of the mean recirculation region dramatically increases

leading to a much better agreement with experimental data of the mean flow topology and of the pressure distribution on the cylinder side. Therefore, the "paradox" previously raised in the literature that a-priori high-fidelity simulations give results in disagreement with experimental data may be explained by the presence of a perfectly sharp edge in the simulations which is not "realistic" and never exactly reproduced in experiments.

The remarkable impact of the edge rounding on the length of the mean recirculation region is related to its effect on the location at which the roll-up of the detached shear-layer occurs; this is in turn linked with the TKE growth along the shear-layer. It is shown that there is an almost perfect correlation between the location at which the maximum of TKE is reached and the length of the mean recirculation region. In particular, the edge rounding leads to a slower growth of TKE and hence to a longer recirculation region. The faster growth of TKE for the sharp-edge case is plausibly due to a larger amount of TKE introduced at separation, as found in our simulations, which mainly originates from larger fluctuations occurring in the boundary layer on the front face near the edge. If these velocity fluctuations are not artificially damped by numerical or eddy viscosity, as e.g. in LES with fine grid resolution and low SGS viscosity, they lead to a too fast growth of TKE and, hence, to a too short mean recirculation length. The analysis of the production term in the TKE equation confirms a much larger production of TKE in the zone immediately after the shear-layer separation for the sharp-edge case.

From a practical viewpoint, these results suggest that for a proper comparison between simulations and experiments for these kind of flows (sep-

aration at the front edges and reattachment on the body surface), specific actions should be adopted. As for the experiments, it would be useful if data on edge rounding or, at least, fabrication tolerances on experimental models were provided. On the other hand, care is needed in the treatment of the upstream edges in numerical simulations. If data on the actual radius of curvature of the real geometry are available, the rounding should be included in the simulation. Otherwise, specific numerical/analytical treatments aimed at reducing the observed effects of sharp edges, which at least when comparing with experiments seem to be unrealistic, could be adopted. A possibility is to damp these effects by numerical or eddy viscosity; however, it is quite complex to find the "optimal" value of the introduced dissipation especially if no reference data are available and, in any case, this requires successive calibrations, which in turn imply huge computational costs for eddy-resolving numerical simulations, like LES or DNS. By the way, as a future work, it would be interesting to ascertain whether the extremely high sensitivity of LES results to numerical resolution and SGS dissipation, observed in previous works, is also an artifact of the presence of perfectly sharp edges and whether the LES results for rounded edges are conversely more reliable. On the other hand, one may wonder whether in some real applications in wind engineering, in which the radius of curvature of the edges is even lower than the values considered herein, the numerical solution obtained for a perfect sharp edge may instead be representative of the real flow. As a future work it could be interesting to investigate also smaller values of the curvature radius to check whether there is some limit value under which the flow becomes similar to that obtained for a perfectly sharp edge. Moreover, in many practical

cases, as a result of manufacturing processes, the radius of curvature may vary in the spanwise direction. The investigation of corner rounding varying in the spanwise direction could also be an interesting topic for future studies.

References

[1] Bartoli G., Bruno L., Buresti G., Ricciardelli F., Salvetti M. V. and Zasso A.: BARC overview document. Available at: http://www.aniv-iawe.org/barc, (2008).

[2] Bruno L., Salvetti M. V. and Ricciardelli F.: Benchmark on the aerodynamics of a rectangular 5:1 cylinder: and overview after the first four years of activity, *J. Wind Eng. Ind. Aerodyn.*, **126**, 87-106, (2014).

[3] Mariotti A., Salvetti M. V., Shoebi-Omrani P. and Witteveen J. A. S.: Stochastic analysis of the impact of freestream conditions on the aerodynamics of a rectangular 5:1 cylinder, *Comput. Fluids* **136**, 170-192, (2016).

[4] Mannini C., Marra A.M., Pigolotti L. and Bartoli G.: The effects of free-stream turbulence and angle of attack on the aerodynamics of a cylinder with rectangular 5:1 cross section, *J. Wind Eng. Ind. Aerodyn.*, **161**, 42–58, (2017).

[5] Mariotti A., Siconolfi L. and Salvetti M. V.: Stochastic sensitivity analysis of large-eddy simulation predictions of the flow around a 5:1 rectangular cylinder, *Eur. J. Mech. B-Fluid*, **62**, 149-165, (2017).

[6] Ricci M., Patruno L., de Miranda S., Ubertini F.: Flow field around a 5:1 rectangular cylinder using LES: Influence of inflow turbulence conditions, spanwise domain size and their interaction. *Computers and Fluids*, 149, 181-193, (2017).

[7] Cimarelli A., Leonforte A., Angeli D.: Direct numerical simulation of the flow around a rectangular cylinder at a moderately high Reynolds number. *Journal of Wind Engineering and Industrial Aerodynamics*, 174, 39-49, (2018).

[8] Moore D., Letchford C. and Amitay, M.: Energetic scales in a bluff body shear layer. *Journal of Fluid Mechanics*, 875, 543-575, (2019). doi:10.1017/jfm.2019.480

[9] Kiya M., Sasaki K.: Free-stream turbulence effects on separation bubble. *J. Wind Eng. Ind. Aerodyn.*, 14 (1-3), 375-398, (1983).

[10] Bruno L., Coste N. and Fransos D.: Simulated flow around a rectangular 5:1 cylinder: spanwise discretisation effects and emerging flow features, *J. Wind Eng. Ind. Aerodyn.*, **104-106**, 203-215, (2012).

[11] Mannini C., Šoda A., Schewe G.: Numerical investigation on the three-dimensional unsteady flow past a 5:1 rectangular cylinder. *Journal of Wind Engineering and Industrial Aerodynamics*, 99 (4), 469-482, (2011).

[12] Cao Y., Tamura T.: Supercritical flows past a square cylinder with rounded corners. *Phys. Fluids*, 29 (8), 085110, (2017).

[13] Van Hinsberg N.P., Schewe G., Jacobs M.: Experiments on the aerodynamic behaviour of square cylinders with rounded corners at Reynolds numbers up to 12 million. *J. Fluids Struct.*, 74, 214–233, (2017).

[14] Van Hinsberg N.P., Schewe G., Jacobs M.: Experimental investigation on the combined effects of surface roughness and corner radius for square cylinders at high Reynolds numbers up to 107. *Journal of Wind Engineering and Industrial Aerodynamics*, 173, 14-27, (2018).

[15] Lamballais E., Silvestrini J., Laizet S.: Direct numerical simulation of flow separation behind a rounded leading edge: Study of curvature effects, *International Journal of Heat and Fluid Flow*, 31 (3), 295-306, (2010).

[16] Xiu D. and Karniadakis G. E.: The Wiener-Askey polynomial chaos for stochastic differential equations. *SIAM Journal on Scientific Computing*, 24(2), 619-644, (2002).

[17] Fischer P. F., Lottes J. W. and Kerkemeier S. G.: Nek5000 Web page. (2008).

[18] Maday Y., Patera A.T., Rønquist E.M.: An Operator-integration-factor splitting method for time-dependent problems: Application to incompressible fluid flow. *Journal of Scientific Computing*, 5 (4), pp. 263-292, (1990).

[19] Fisher P. and Mullen J.: Filter-based stabilization of spectral element methods. *C. R. Acad. Sci. I-Math.* 332 (1), 265-270, (2001) .

[20] Domarazdki J. A.: Large eddy simulations without explicit eddy viscosity models. *Int. J. Comput. Fluid Dyn.*, 24 (10), 435-447, (2010).

[21] Mathew J., Lechner R., Foysi H., Setsterhenn J. and Friedrich R.: An explicit filtering method for large eddy simulation of compressible flows. *Phys. Fluids*, 15, 2279-2289, (2003).

[22] Mannini, C., Mariotti, A., Siconolfi, L. and Salvetti, M.V.: Benchmark on the aerodynamics of a 5:1 Rectangular cylinder: Further experimental and LES results, in: Salvetti M., Armenio V., Fröhlich J., Geurts B., Kuerten H. (eds) Direct and Large-Eddy Simulation XI. *ERCOFTAC Series*, Springer, Cham, **25**, 427-432, (2019).

[23] Matsumoto M., Shirato H., Aaraki K., Haramura T., Hashimoto, T.: Spanwise coherence characteristic of surface pressure field on 2D bluff bodies, *Journal of Wind Engineering and Industrial Aerodynamics*, 91, 155-163, (2003).

[24] Cimarelli A., Leonforte A., De Angelis E., Crivellini A., Angeli D.: On negative turbulence production phenomena in the shear layer of separating and reattaching flows, *Physics Letters A*, 383,10, 1019-1026, (2019). https://doi.org/10.1016/j.physleta.2018.12.026.

[25] Mariotti A., Buresti G.: Experimental investigation on the influence of boundary layer thickness on the base pressure and near-wake flow features of an axisymmetric blunt-based body, *Exp Fluids*, 54, 1612, (2013).

[26] Mariotti A., Buresti G., Gaggini G., Salvetti M.V.: Separation control and drag reduction for boat-tailed axisymmetric bodies through contoured transverse grooves, *Journal of Fluid Mechanics*, 832, 514-549, (2017).

[27] Mariotti A.: Axisymmetric bodies with fixed and free separation: base pressure and near-wake fluctuations, *Journal of Wind Engineering and Industrial Aerodynamics*, 176, 21-31, (2018).

[28] Winant C. D., Browand F. K.: Vortex pairing: the mechanism of turbulent mixing-layer growth at moderate Reynolds number, *Journal of Wind Engineering and Industrial Aerodynamics*, 63, 237-255 (1974).

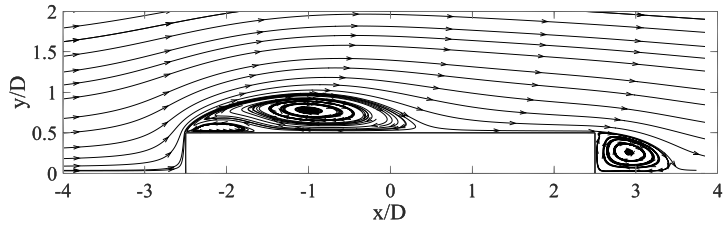

(a) $r/D = 0$

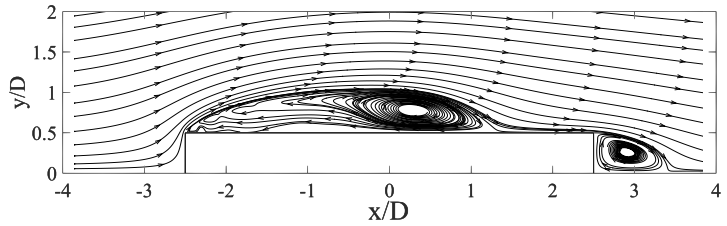

(b) $r/D = 0.0037$

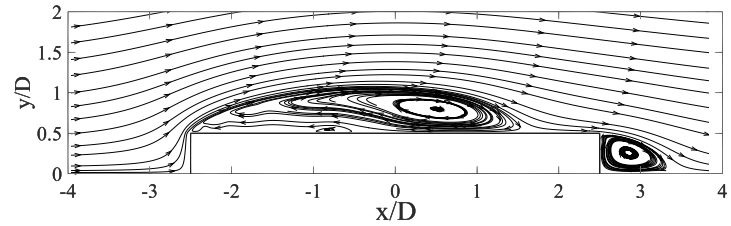

(c) $r/D = 0.0177$

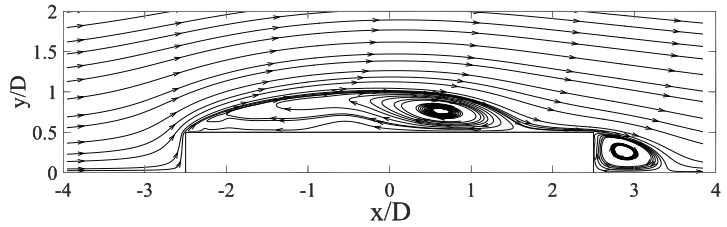

(d) $r/D = 0.036$

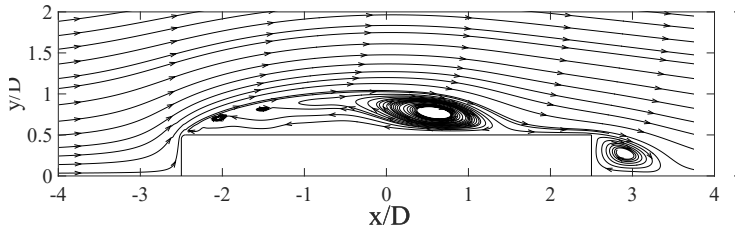

(e) $r/D = 0.05$

Figure 5: Time- and span-averaged streamlines. Comparison between the sharp-edge simulation $r/D = 0$ and the simulations for the different values of the curvature radius.

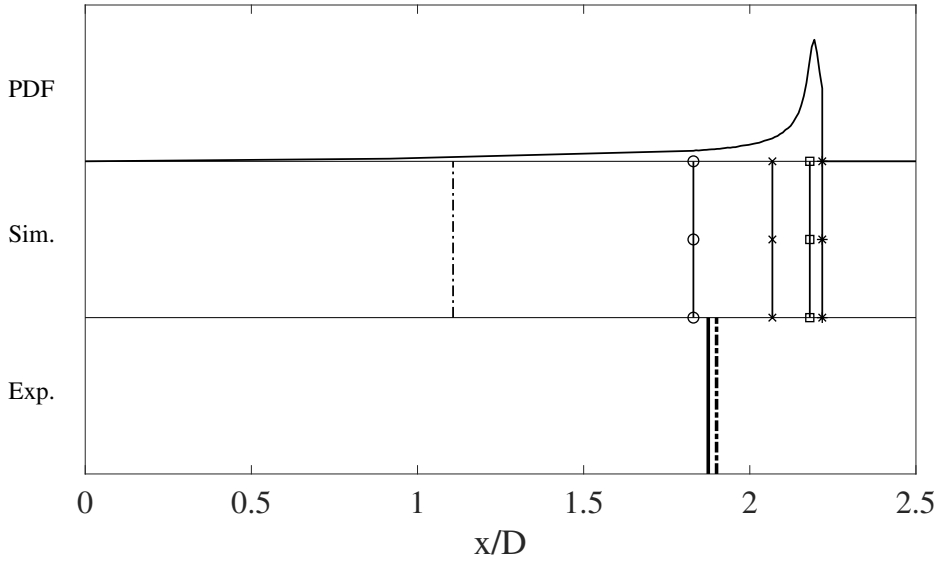

Figure 6: Mean reattachment location along the cylinder lateral side. Lower panel: experiments by Matsumoto et al. [23] (-·-) and by Moore et al. [8] (solid line). Middle panel: reattachment point for the sharp-edges simulations (-·-) and for the rounding edges $r/D = 0.0037$ ($\bigcirc$), $r/D = 0.0177$ ($\times$), $r/D = 0.036$ ($\square$) and $r/D = 0.05$ ($*$). Top panel: PDF of x_r.

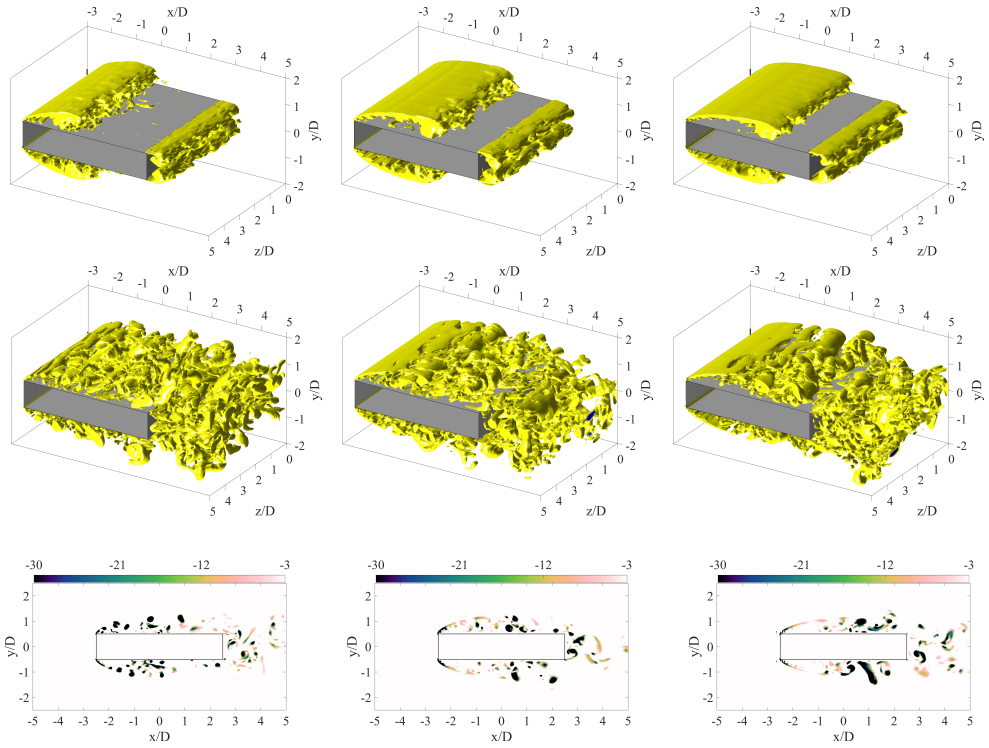

(a) $r/D = 0$ (b) $r/D = 0.0037$ (c) $r/D = 0.05$

Figure 7: Isosurfaces of the time-averaged vortex indicator λ_2 (first row), isosurfaces of the instantaneous vortex indicator λ_2 (second row) and instantaneous vortex indicator λ_2 on the plane $z = 0$ (third row) for $r/D = 0$, $r/D = 0.0037$ and $r/D = 0.05$.

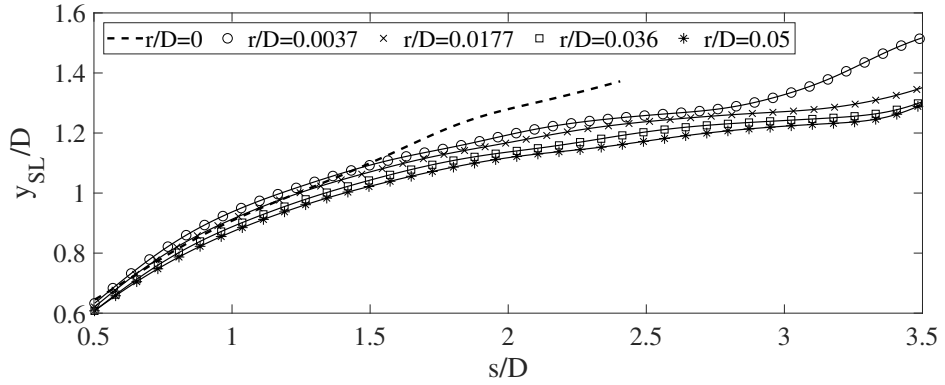

(a)

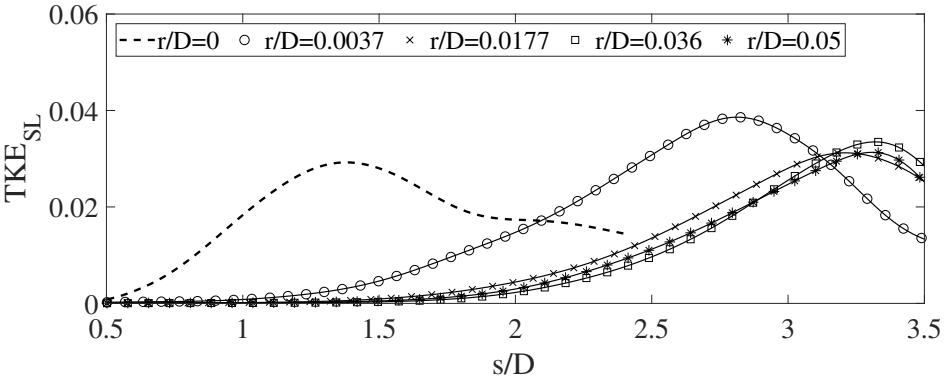

(b)

Figure 8: Wall-normal position of the mean shear-layer edge (a) and sampling of the turbulent kinetic energy along it (b). $r/D = 0$ (- -), $r/D = 0.0037$ ($\bigcirc$), $r/D = 0.0177$ ($\times$), $r/D = 0.036$ ($\square$) and $r/D = 0.05$ ($*$).

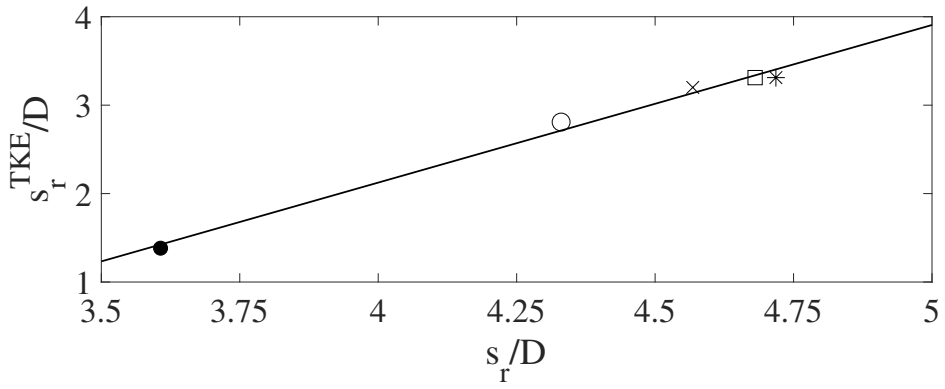

Figure 9: Correlation of the location of the TKE maximum (s_r^{TKE}/D) with the reattachment point location on the cylinder side (s_r/D). $r/D = 0$ (•), $r/D = 0.0037$ (◯), $r/D = 0.0177$ (×), $r/D = 0.036$ (□) and $r/D = 0.05$ (∗).

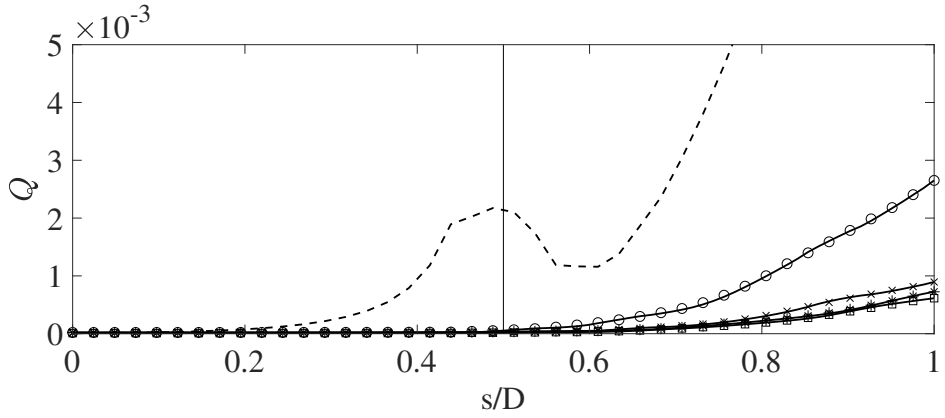

Figure 10: Integral of the turbulent kinetic energy Q against the local curvilinear abscissa (s/D). $r/D = 0$ (- -), $r/D = 0.0037$ (◯), $r/D = 0.0177$ (×), $r/D = 0.036$ (□) and $r/D = 0.05$ (∗). The vertical black line is placed at $s/D = 0.5$.

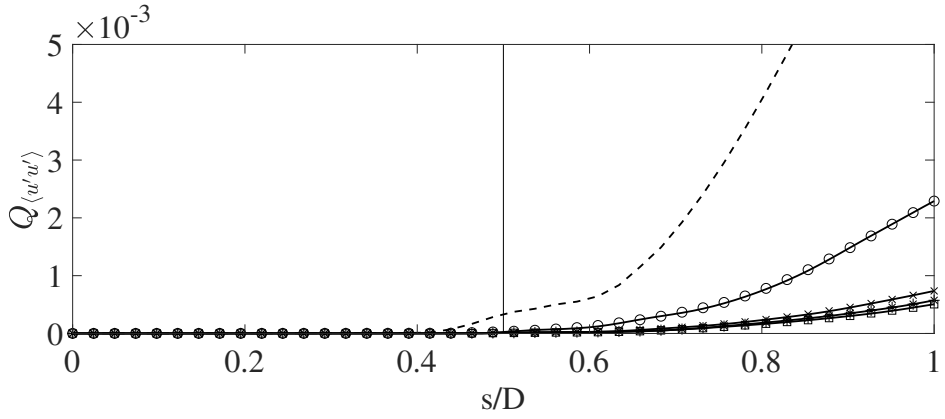

(a)

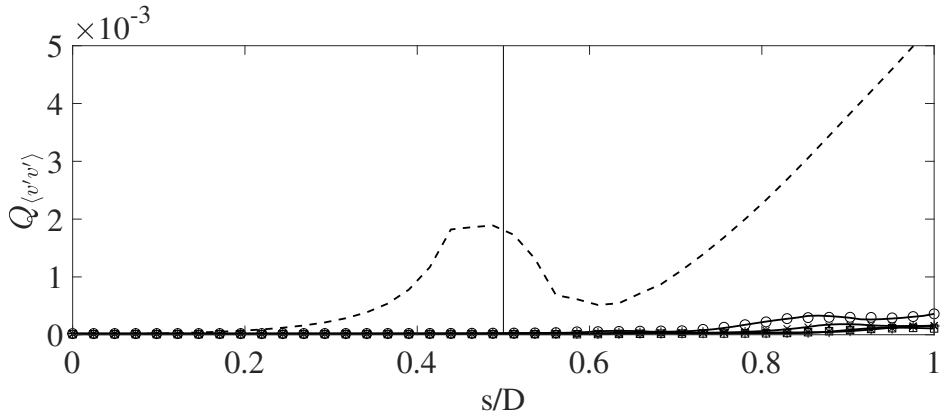

(b)

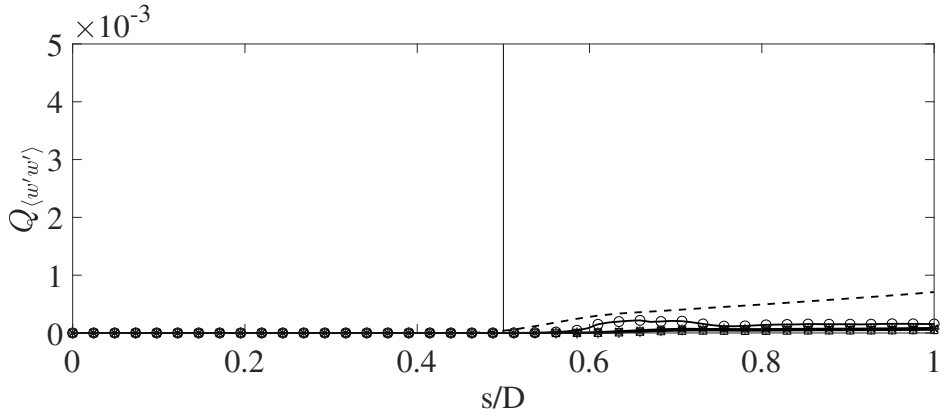

(c)

Figure 11: Integral of the turbulent kinetic energy components against the local curvilinear abscissa (s/D): (a) $Q_{\langle u'u'\rangle}$, (b) $Q_{\langle v'v'\rangle}$ and (c) $Q_{\langle w'w'\rangle}$. $r/D = 0$ (- -), $r/D = 0.0037$ (◯), $r/D = 0.0177$ (×), $r/D = 0.036$ (□) and $r/D = 0.05$ (∗). The vertical black line is placed at $s/D = 0.5$.

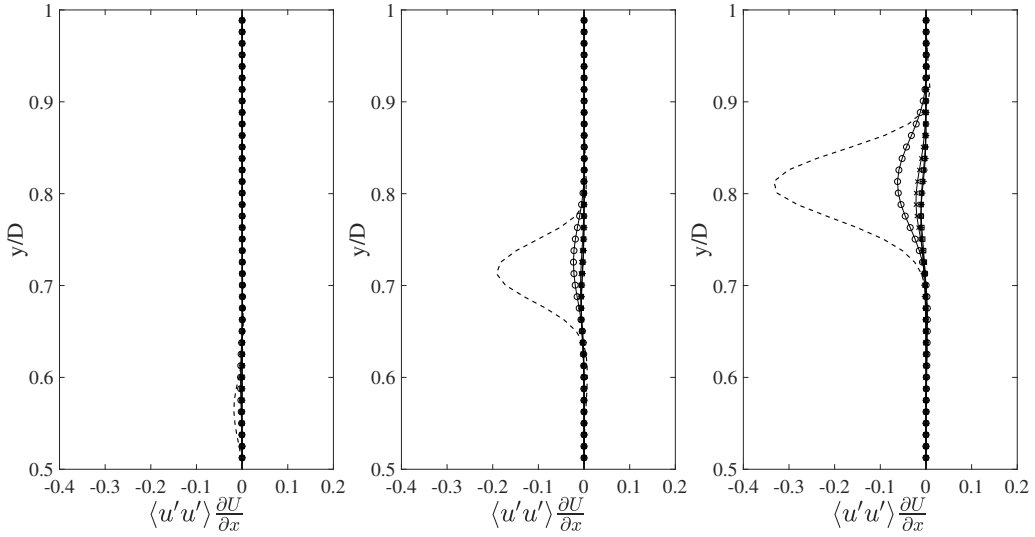

(a) $x/D = -2.5$ (b) $x/D = -2.3$ (c) $x/D = -2.1$

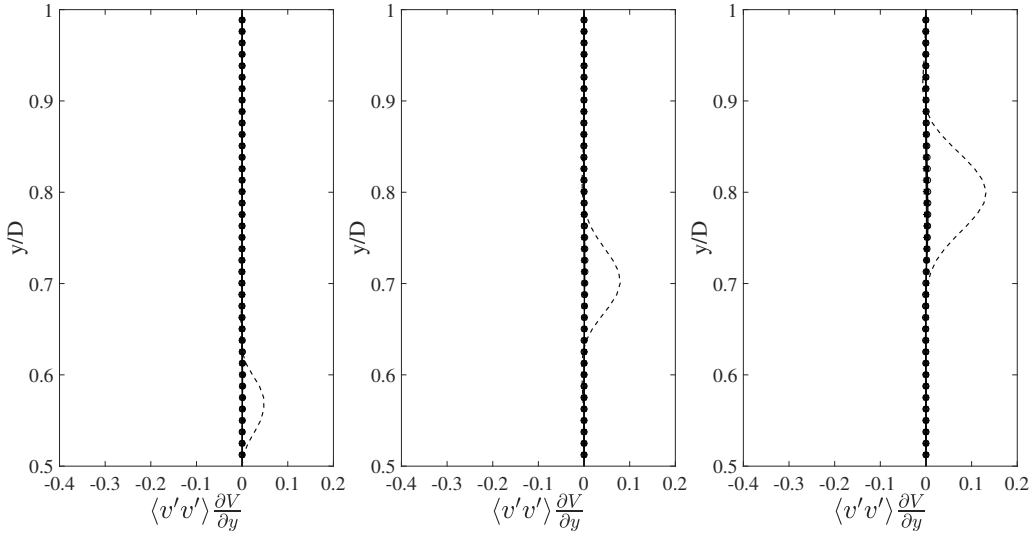

(d) $x/D = -2.5$ (e) $x/D = -2.3$ (f) $x/D = -2.1$

Figure 12: Contributions to $-\mathcal{P}$ at different streamwise positions along the lateral side of the cylinder. (a)-(c) $\langle u'u' \rangle \frac{\partial U}{\partial x}$ component and (d)-(f) $\langle v'v' \rangle \frac{\partial V}{\partial y}$ component. $r/D = 0$ (- -), $r/D = 0.0037$ ($\bigcirc$), $r/D = 0.0177$ ($\times$), $r/D = 0.036$ ($\square$) and $r/D = 0.05$ ($*$).

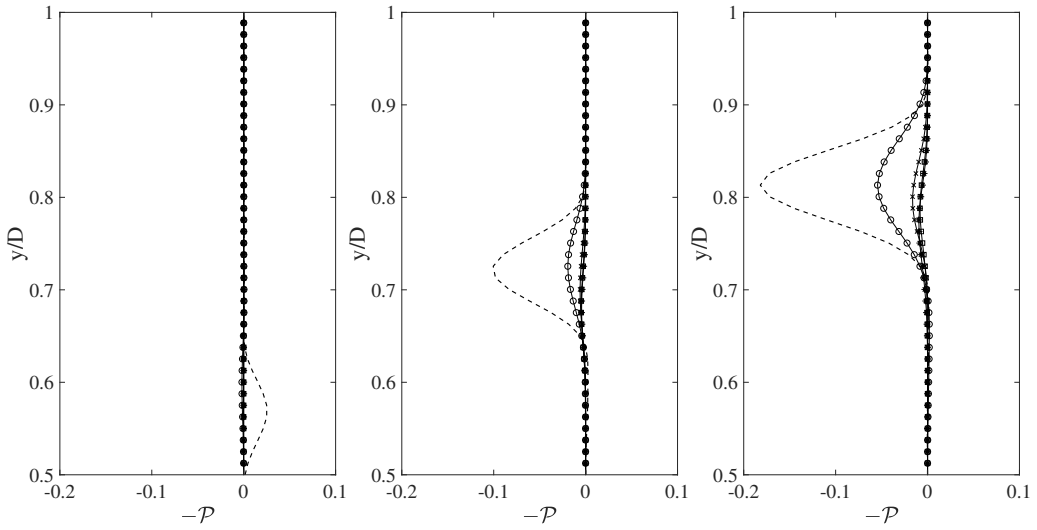

(a) $x/D = -2.5$ (b) $x/D = -2.3$ (c) $x/D = -2.1$

Figure 13: Opposite of the TKE production term, $-\mathcal{P}$, at different streamwise positions along the lateral side of the cylinder. $r/D = 0$ (- -),$r/D = 0.0037$ ($\bigcirc$), $r/D = 0.0177$ ($\times$), $r/D = 0.036$ ($\square$) and $r/D = 0.05$ ($*$).

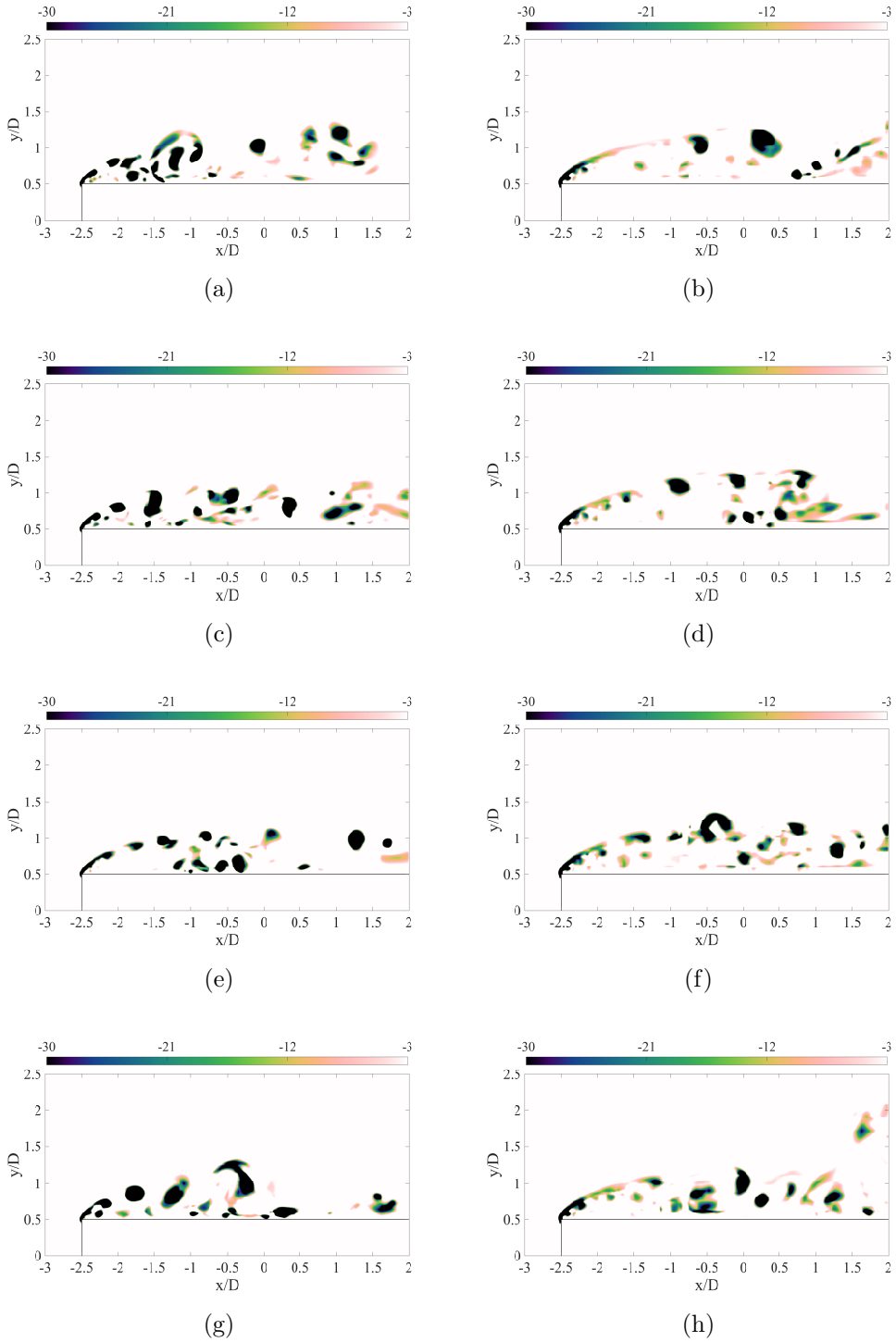

Figure 14: Instantaneous vortex indicator λ_2 on the plane $z = 0$ for $r/D = 0$ (left column) and $r/D = 0.0037$ (right column) at four different times.

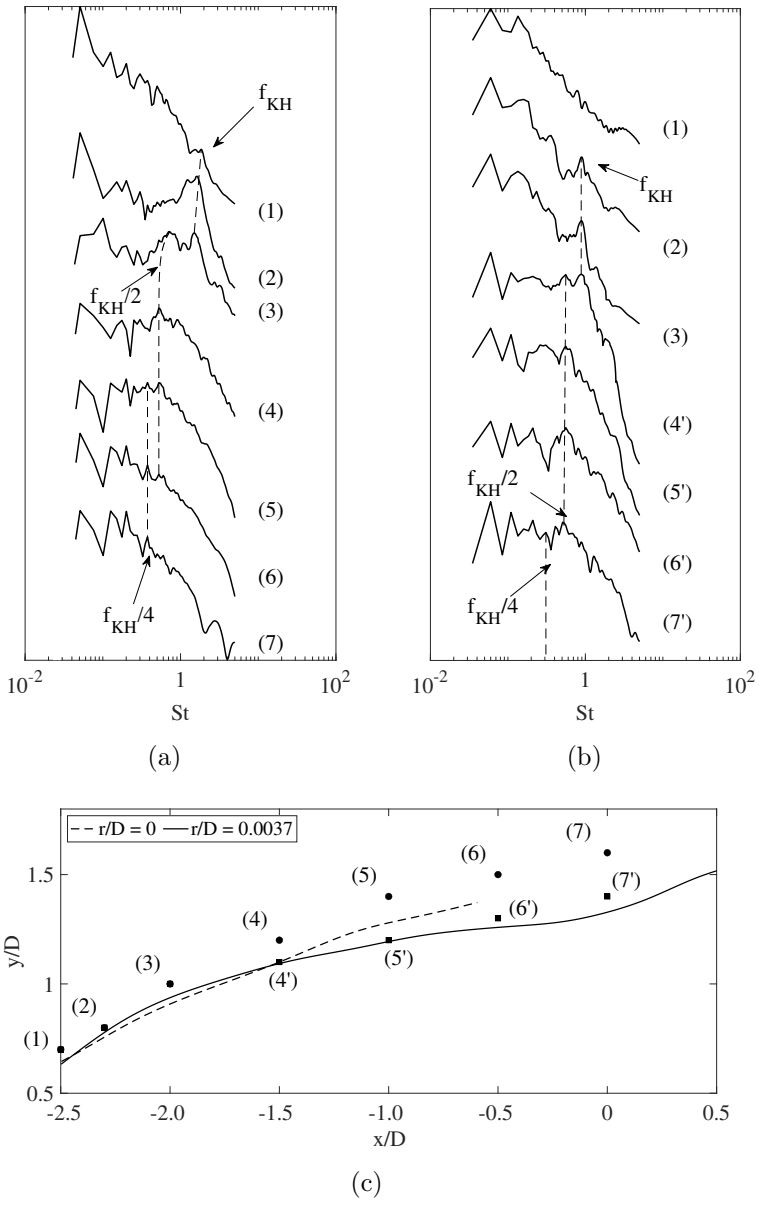

Figure 15: Distributions of power spectral density of velocity fluctuations near separation for (a) $r/D = 0$ and (b) $r/D = 0.0037$. Spectral density amplitudes have been linearly shifted on the ordinate to permit the comparison of the energy distribution between probes (1) and (7). (c) Probe positions in relation to the time-averaged shear-layer edges for $r/D = 0$ (- -) and $r/D = 0.0037$ (—).

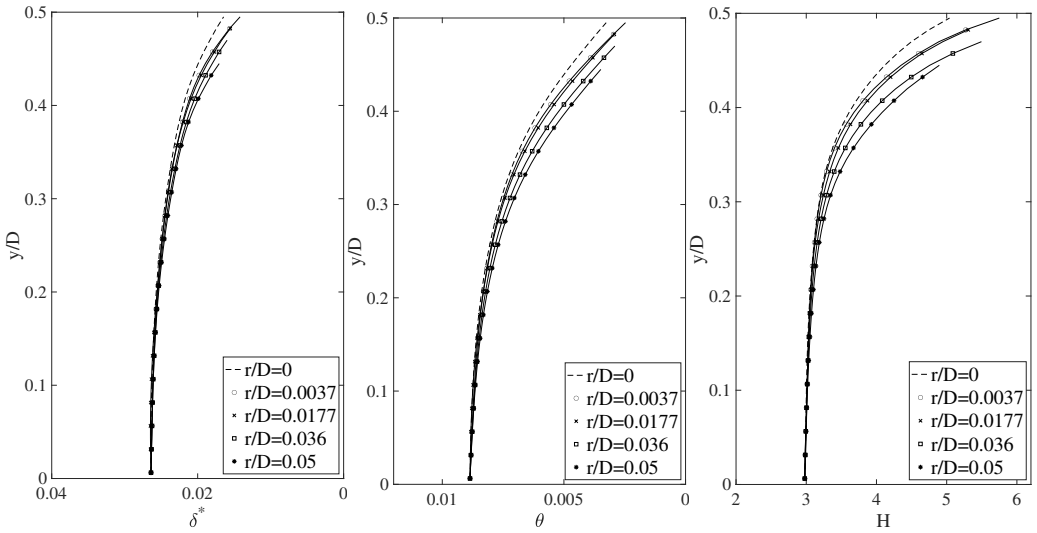

Figure 16: Boundary layer characteristics on the front face of the rectangular cylinder: (a) displacement thickness, (b) momentum thickness and (c) shape factor. $r/D = 0$ (- -),$r/D = 0.0037$ ($\bigcirc$), $r/D = 0.0177$ ($\times$), $r/D = 0.036$ ($\square$) and $r/D = 0.05$ ($*$).